Dynamically Unveiling Metal-Nitrogen Coordination during Thermal Activation to Design High-Efficient Atomically Dispersed CoN_4 Active Sites

Yanghua He[1,Δ], Qiurong Shi[1,Δ], Weitao Shan[2,Δ], Xing Li[3], A. Jeremy Kropf[4], Evan C. Wegener[4], Joshua Wright[5], Stavros Karakalos[6], Dong Su[3], David A. Cullen[7,*], Guofeng Wang[2,*], Deborah J. Myers[4,*], and Gang Wu[1,*]

Abstract: Atomically dispersed CoN_4 site catalysts are more desirable than FeN_4 site catalysts to enhance catalyst stability and mitigate Fenton reactions during the oxygen reduction reaction (ORR). However, the lack of an understanding of CoN_x active site formation during the critical thermal activation makes the rational catalyst design impossible. Here, we elucidate the structural evolution of CoN_4 sites during thermal activation by developing a zeolitic imidazolate framework (ZIF)-8-derived carbon host as an ideal model for Co^{2+} ion adsorption. Subsequent *in-situ* X-ray absorption spectroscopy analysis can dynamically track inactive Co-OH and Co-O species' conversion into active CoN_4 sites. The critical transition occurs at ~700°C and becomes optimal at 900°C, generating the highest intrinsic activity and four-electron selectivity. Density functional theory (DFT) calculations elucidate that the ORR is kinetically favored by the thermal-induced compressive strain of Co-N bonds in CoN_4 active sites formed at 900 °C. Inspired by the new understanding, we developed a two-step chemical pre-doping and adsorption approach to designing a Co-N-C catalyst with increased CoN_4 site density and optimized porosity for mass transport, and demonstrated outstanding proton-exchange membrane fuel cell performance and durability.

Introduction

Atomically dispersed and nitrogen-coordinated MN_4 sites (M = Fe, Co, Ni, Cu, Cr, Ce, or Mn) in pyrolyzed carbon (M-N-C) catalysts are the most promising platinum-group metal (PGM)-free catalysts for oxygen reduction reaction (ORR),[1-4] CO_2 reduction,[5-6] and other electrocatalysis.[7-10] However, despite the most encouraging ORR activity obtained with Fe-N-C catalysts,[11-17] their unsatisfied stability is the major barrier for vital applications.[18] Even worse, the Fenton reactions between Fe^{2+} and H_2O_2 are significant concerns due to the generation of radical oxygen species (ROS).[19-21] Both ROS and H_2O_2 could attack the MN_4 active sites, carbon support, organic ionomers, and polymer membranes, thereby accelerating performance degradation.[22-24] An alternative Co-N-C catalyst, which does not significantly promote Fenton reactions, has recently garnered attention due to significant improvements in ORR activity and stability in acidic electrolytes (**Table S1**),[25-30] and, most importantly, encouraging fuel cell power density and performance durability.[14, 28-29, 31-34]

Despite the significant progress in improving Co-N-C catalysts' catalytic activity and stability via empirical engineering of the composition and structure,[25] the fundamental understanding of CoN_4 site formation mechanism remains unknown for decades. This is primarily due to the complexity of the processes occurring during the critical high-temperature pyrolysis step, involving the simultaneous carbonization of carbon structure, nitrogen doping, and the CoN_4 site generation. Unveiling the CoN_4 active site evolution process during the thermal activation is pivotal to illustrate the relationship between Co-N atomic configuration and activity and selectivity towards the four-electron ORR. The in-depth understanding offers valuable guidance toward the efficient and targeted synthesis of high-performance Co-N-C catalysts for various energy conversion technologies.[2, 16, 35-37]

In this work, we firstly elucidated the CoN_4 active site evolution mechanism under controlled thermal activation by developing a nitrogen-doped carbon model host derived from zeolitic imidazolate framework-8 (ZIF-8) for Co ion adsorption. Employing this carbon host could effectively exclude the interference from the complex carbonization and nitrogen doping processes, providing the benefit of precise control of Co-N coordination and local carbon structures. This well-defined and straightforward system is desirable to exclusively determine the Co-N bond structure relevant to intrinsic activity and selectivity, which only depends on thermal activation temperatures.

---

[1] Y. He[Δ], Q. Shi[Δ], Prof. G. Wu*
Department of Chemical and Biological Engineering, University at Buffalo, The State University of New York, Buffalo, NY 14260, United States
E-mail: gangwu@buffalo.edu (G. Wu)

[2] W. Shan[Δ], Prof. G. Wang*
Department of Mechanical Engineering and Materials Science, University of Pittsburgh, Pittsburgh, PA 15261, United States
E-mail: guw8@pitt.edu (G. F. Wang)

[3] Dr. X. Li, Dr. Su
Center for Functional Nanomaterials, Brookhaven National Laboratory, Upton, NY 11973, United States

[4] Dr. A. J. Kropf, Dr. E. C. Wegener, Dr. D. J. Myers
Chemical Sciences and Engineering Division, Argonne National Laboratory, Lemont, IL 60439, United States
Email: dmyers@anl.gov (D. J. Myers)

[5] Prof. J. Wright
Illinois Institute of Technology. Chicago, IL 60616, United States

[6] Prof. S. Karakalos
Department of Chemical Engineering, University of South Carolina, Columbia, SC 29201, United States

[7] Dr. D. A. Cullen
Materials Science and Technology Division, Oak Ridge National Laboratory, Oak Ridge, TN, 37831 United States
Email: cullenda@ornl.gov (D. A. Cullen)

[Δ] These authors contributed equally to this work.

Supporting information for this article is given via a link at the end of the document.

Utilizing *in-situ* X-ray absorption spectroscopy (XAS) and atomic-resolution electron microscopy, we found that thermal activation at 700°C can initiate active CoN_4 sites, and the optimal CoN_4 sites are accomplished at 900 °C. Furthermore, first-principle density functional theory (DFT) calculations elucidated that thermal-induced Co-N local strain in the CoN_{2+2} and CoN_4 sites is responsible for the experimentally-observed ORR activity enhancement at >700 °C. Motivated with this understanding, we designed a two-step chemical Co doping and adsorption strategy to increase the CoN_4 site density and optimize catalyst morphology for promoting mass transport. This Co-N-C catalyst, therefore, exhibited much-enhanced ORR activity and four-electron selectivity in challenging acidic electrolytes. We further demonstrated the two-step Co-N-C catalyst with promising performance and durability in H_2/air proton-exchange membrane fuel cells (PEMFCs).

Results and Discussion

2.1 Design catalyst models *via* one-step adsorption

As illustrated in **Figure 1a**, we developed the ion adsorption method to elucidate the CoN_4 active site formation process by varying thermal activation temperatures. Firstly, nitrogen-doped porous carbon (ZIF-NC) was prepared by carbonizing ZIF-8 precursors at 1100 °C for one hour under Ar flow. During the high-temperature pyrolysis, the organic hydrocarbon linkers were directly carbonized to a N-doped carbon skeleton. Due to a low boiling point of zinc at 907°C, the simultaneous zinc evaporation yielded a high-surface-area and porous carbon host. As verified by Brunauer-Emmett-Teller (BET) surface area measurements (**Figure S1a**), pore distribution plots (**Figure 1b**), and the nitrogen adsorption-desorption isothermal curves (**Figure S1b**), the ZIF-NC host retained the high surface area (920 m^2 g^{-1}) and large micropore volume (0.373 cm^3 g^{-1}) from the ZIF-8 nanocrystal precursor (**Table S2**). After the controlled Co^{2+} ion adsorption, the carbon host's N-riched defects can readily trap adsorbed Co^{2+} ions, providing a stabilizing force against aggregation. X-ray diffraction (XRD) patterns (**Figure 1c**), Raman spectra (**Figure 1d**, **S2,** and **Table S3**), and X-ray photoelectron spectroscopy (XPS) analysis (**Figure S3** and **Table S4-S6**) indicate that the carbon structure and nitrogen doping in the carbon host kept unchanged up to 1100 °C. This further evidenced that the highly stable carbon host is ideal for studying the CoN_4 active sites' formation mechanism by correlating the Co-N coordination structures and their catalytic properties

The ZIF-NC-Co-room temperature (RT) sample was typically formed by adsorbing $Co(NO_3)_2$ into ZIF-NC nanoparticles followed by drying under vacuum. The ZIF-NC-Co-RT was subsequently heat-treated at various temperatures (300 to 1100 °C) to prepare a series of samples (ZIF-NC-Co-T), which can track the Co-N structural evolution. Separating the complicated carbonization and nitrogen doping processes from the critical thermal activation makes the ZIF-NC model system desirable for exclusively studying CoN_4 active sites.

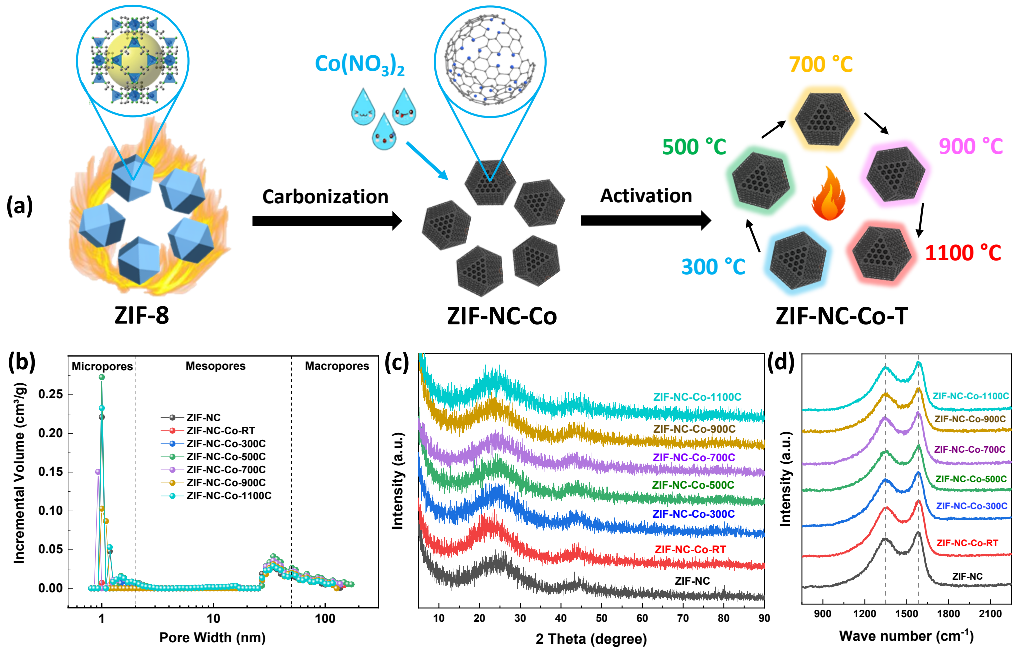

Figure 1. (a) Precise synthesis control strategy to elucidate the CoN_4 site formation process. Structure evolution of ZIF-NC carbon hosts during Co ion adsorption and subsequent thermal activation at different temperatures illustrated by (b) pore size distributions, (c) XRD patterns, and (d) Raman spectra.

2.2 Investigation of CoN_4 site evolution

ORR activity of various ZIF-NC-Co-*T* (*T* = 300 to 1100°C) catalysts was measured in O_2-saturated 0.5 M H_2SO_4 electrolyte to elucidate the thermal activation's role in forming active CoN_4 sites. (**Figure 2a**). Without Co doping, the ZIF-NC host showed poor ORR activity with an onset potential (E_{onset}) of 0.80 V and a half-wave potential ($E_{1/2}$) of 0.62 V under the defined testing conditions. This is typical

ORR activity for “metal-free” C-N_x active sites in acids.[38] The $E_{1/2}$ of the ZIF-NC-Co-RT even showed a negative shift after the adsorption of Co^{2+} ions, probably due to the blockage of micropores by the adsorbed Co compounds, as evidenced in **Figure 1b** and **Table S2**. However, the micropore volumes recovered quickly following a thermal activation, suggesting that Co ions/salts were first located in the micropores and then gradually decomposed into atomically-dispersed species. A relatively low temperature of 700 °C is sufficient to initiate a substantial increase in ORR activity, with $E_{1/2}$ reaching 0.73 V, indicating that this temperature is critical for forming active CoN_4 sites. ZIF-NC-Co-Ts’ ORR activity was further improved with an increase of activation temperature up to 900 °C, reaching an $E_{1/2}$ of 0.81 V. However, a higher temperature of 1100 °C led to decreased ORR activity.

The H_2O_2 yield during the ORR was also measured using a rotating ring-disk electrode (RRDE) to determine the catalyst's four-electron selectivity to H_2O (**Figure 2b**). The Co-free ZIF-NC sample exhibited a high H_2O_2 yield of approximately 15%, whereas the ZIF-NC-Co-900 and -1100 catalysts demonstrated negligible H_2O_2 yield (< 1%), indicating the nearly complete reduction of O_2 to H_2O instead of H_2O_2. This ultra-low H_2O_2 yield is significantly different from the previous Co-N-C catalyst derived from polyaniline[39-40], suggesting a new type of Co active sites.

To determine that the ORR activity arose from CoN_4 moieties rather than CN_x species, ZIF-NC-Na^+-*T* samples obtained via adsorbing $NaNO_3$ were prepared for comparison. **Figure 2c** reveals that CoN_4 species were the dominant active sites in these ZIF-NC-Co-*T* catalysts because ZIF-NC-Na^+-*T* samples with identical thermal activation exhibited vastly inferior ORR activity similar to C-N_x active sites.

The steady-state ORR polarization plots for ZIF-NC-*x*Co-900C catalysts, derived from various adsorbed $Co(NO_3)_2$ contents, treated at the optimal 900 °C, are shown in **Figure 2d.** These results provide evidence that the increased number of CoN_x sites are responsible for the enhanced ORR activity. The Co-free ZIF-NC-0Co-900C sample showed the lowest catalytic activity, corresponding to the N-doped carbon host activity. The ORR activity of the ZIF-NC-*x*Co-900C samples initially showed a positive correlation with Co content, following the order of ZIF-NC-1Co < ZIF-NC-5Co < ZIF-NC-10Co. It suggests that all Co ions can be utilized entirely to form active CoN_4 sites, rising active site density. According to XPS analysis, the Co content of the optimal ZIF-NC-10Co catalyst is 0.5 at.% (**Table S7**). Excessive $Co(NO_3)_2$ adsorption, however, led to decreased activity and formation of inactive Co_3O_4 and Co nanoparticles during the thermal activation at 900°C, as verified by XRD patterns (**Figure S4**), presumably due to the insufficient number of anchoring N sites in the carbon host. Therefore, the appropriate Co content is essential to maximize ORR activity. This strategy demonstrated precise control of active site density for Co-N-C catalysts without altering the carbon structure and morphology (**Figure S5-S6** and **Table S8-S10**).

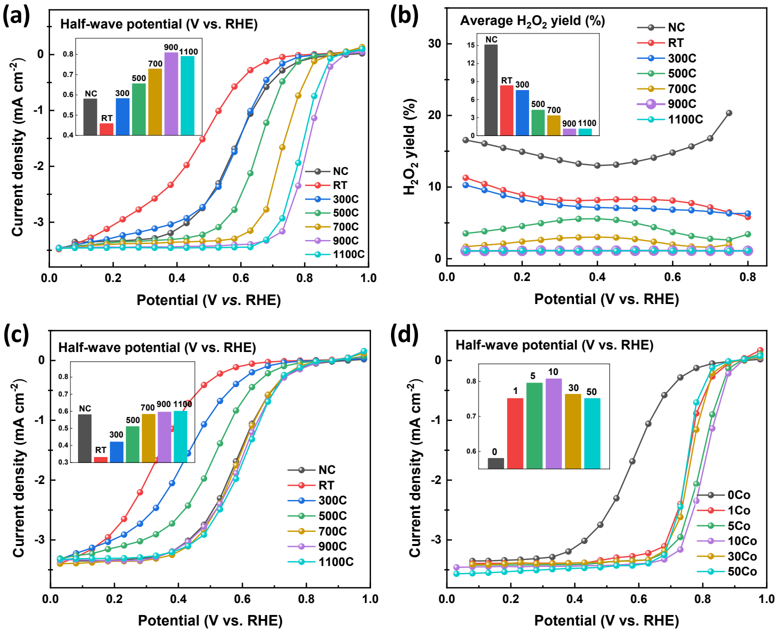

Figure 2. (a) Steady-state ORR polarization plots and (b) H_2O_2 yield of ZIF-NC-Co-T, (c) ZIF-NC-Na^+-T treated at different temperatures, and (d) ZIF-NC-*x*Co-900C with varied Co content in O_2-saturated 0.5 M H_2SO_4 electrolyte with the rotating rate of 900 rpm, where *x* represents the volume of Co solution added in the solvents during the adsorption synthesis step.

Multiple characterization techniques were employed to identify the Co species in various ZIF-NC-Co-*T* samples from different heating temperatures. Firstly, no significant Co-containing crystalline phases were detected in all ZIF-NC-Co-T catalysts according to XRD patterns. The valence state and evolution of the surface composition during the thermal activation were examined using XPS (**Figure S3** and **Table S4-S6**). The ZIF-NC’s N 1s spectrum exhibited two sharp peaks, ascribed to pyridinic-N (398.4 eV) and graphitic-N (401.0 eV) (**Figure S3b**). After the adsorption of Co ions, a new peak (399.6 eV) corresponding to Co-N coordination appeared with a percentage of 13-16% (**Table S6**). The pyridinic-N percentage decreased from 30 at.% to 19 at.% after adsorbing Co^{2+} and slightly increased during the heat treatment. This indicates that pyridinic-N initially bonded with Co ions and formed unstable CoN_x species. During the thermal activation, weak Co-N bonding disappears, which explains the phenomenon of Co-N content in ZIF-NC-Co-RT is higher than that in ZIF-NC-Co-T samples. We have done an in-situ Transmission electron microscope (TEM) test to observe the change of morphology and elements. As shown in **Figure S7**, we found that no apparent changes or particle formation can be observed in HAADF-STEM images during the heating treatment in a wide temperature range, indicating that the aggregates Co species might be insignificant.

Because *ex-situ* XAS will involve changes in the oxidation state due to air exposure during sample handling, storage, and transportation, which are not accurate to determine intermediate states during the active site formation. Therefore, we designed *in situ* XAS experiments for dynamically tracking active sites' evolution during a continuous heat treatment under vacuum. To determine the critical Co-N coordination during thermal activation, *in situ* XAS data were acquired at the Co K-edge for the ZIF-NC-Co-T sample during a heat treatment up to 1100 °C. The near edge region of the XAS spectra was recorded for the ZIF-NC-Co-T at room temperature (**Figure 3a**) and various temperatures during the thermal activation process (**Figure 3b-c** and **Figure S8**). Fits to the EXAFS region of selected spectra are summarized in **Table S11**. The near edge region of the XAS spectra of the catalyst precursor and of several standard compounds (*i.e.,* Co, CoO, $Co(NO_3)_2$ $6H_2O$, and CoPc) are compared in **Figure 3a**. The ZIF-NC-Co-RT and the CoO reference's similar pre-edge energy indicates that Co in the ZIF-NC-Co-RT is in the 2+ oxidation state. The EXAFS spectrum (**Figure 3b**) and fits to the spectrum (**Table S11**) for the ZIF-NC-Co-RT have characteristics similar to those observed for $Co(OH)_2$ brucite of Hong *et al.* and with similar bond distances as those observed by XRD.[41] This observation indicates that hydrated nitrate decomposes or is converted to the hydroxide species during the adsorption process and/or subsequent drying step at 60°C.

The *in situ* XAS data represented in the Fourier transforms of the EXAFS (**Figure 3b)**, the derivative of the XANES region (**Figure 3c),** the XANES data (**Figure S9**), and the fits to the EXAFS data (**Table S11**) show that the Co undergoes a dramatic change in coordination during the thermal treatment at temperatures between 500 °C and 700 °C. The scattering path between 2 and 3 Å in the Fourier transform disappears, and the length of the scattering path between 1 and 2 Å decreases. The length of the scattering path in the Fourier transform of the XAS data taken at ≥700 °C agrees well with that of the CoN_4 phthalocyanine standard. The short first shell bond lengths derived from the EXAFS fits (e.g., 1.90 Å at 800 °C, **Table S11**) agree well with those expected for a square planar CoN_4 complex (Co phthalocyanine: 1.92 Å, **Table S11**). Moreover, the first derivative of the XANES pre-edge data, in particular the feature in the 7710 to 7715 eV energy range, clearly shows the signature 1s→4pz transition of in-plane $Co(II)N_4$ moieties emerge at approximately 700°C (**Figure 3c**). Linear combination fitting of the XANES region of the 700°C spectrum (**Figure S10**) shows that about 29% of the Co is in the metallic state, most likely as Co nanoparticles, and 71% is Co-N_4. At temperatures ≥ 800 °C, CoN_4 is the only Co species present within the detection limit of the technique (**Table S13**, **Figure S9**). The XANES spectrum of Co-N-C at the activation temperature above 700 °C is similar to that observed by Zitolo *et al.*[42] Thus, it matches XANES simulation for Co species in a micropore-hosted porphyrinic coordination environment, *i.e*., CoN_4C_{12} (or its defective derivatives), as shown in **Figure S11**, which used the standard Co(II)-Phthalocyanine (CoPc) consisting of defined CoN_4 structure as a fitting reference (**Figure S12**).

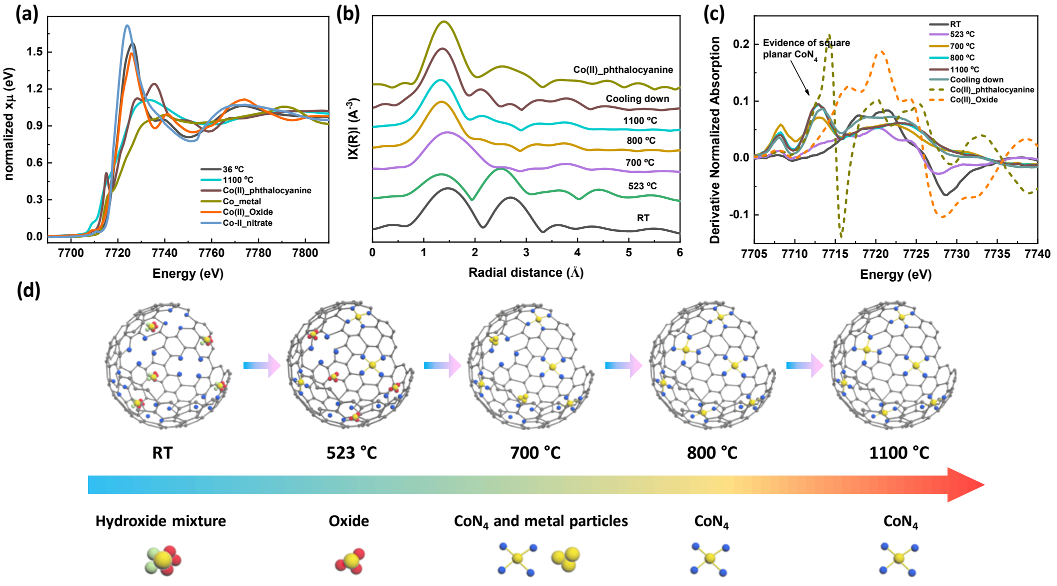

Figure 3. *In situ* (a) Co K-edge X-ray absorption near edge structure (XANES) spectra, (b) Fourier transforms of the Co K-edge extended x-ray absorption fine structure (EXAFS), and (c) derivative of the normalized XANES data for the ZIF-NC-Co acquired at the indicated temperatures during thermal activation. (d) Schematic illustration of the exclusive formation of atomic CoN_4 active sites within a nitrogen-doped carbon host as a function of thermal activation temperature.

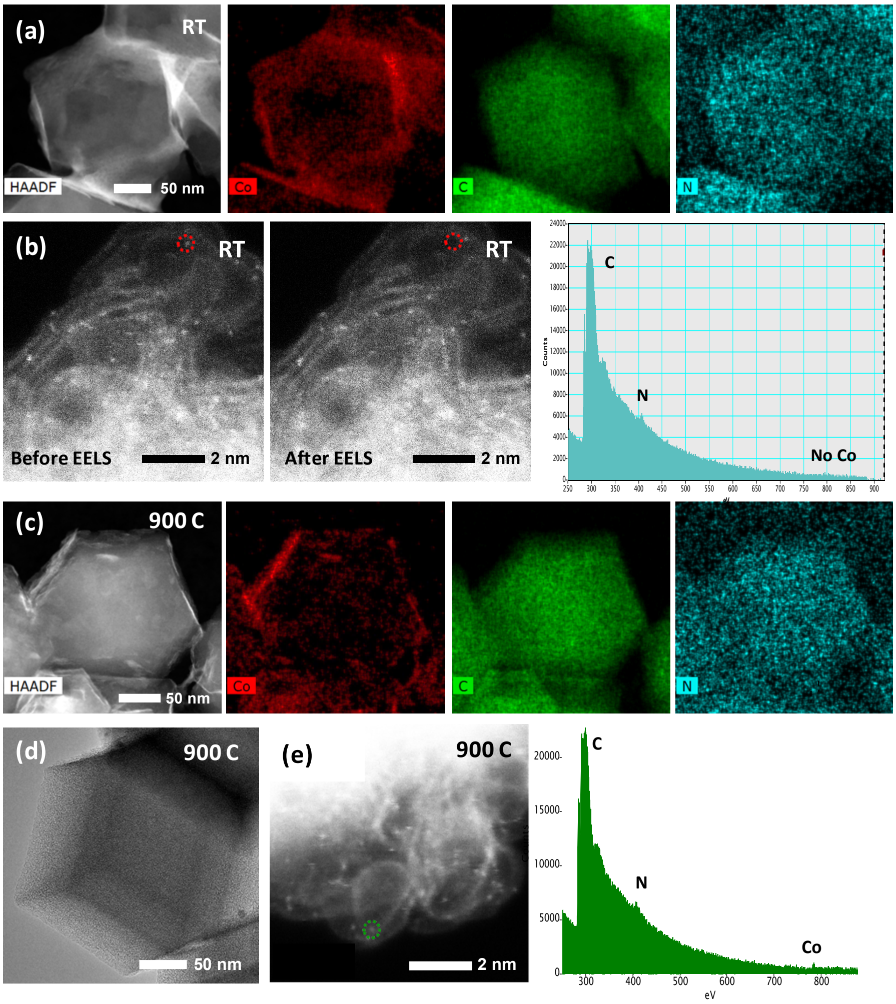

Figure 4. Morphology and atomic structure of (a-b) ZIF-NC-Co-RT and (c-e) ZIF-NC-Co-900C catalyst observed by high-angle annular dark field-scanning transmission electron microscope (HAADF-STEM) images, the scanning transmission electron microscopy with energy-dispersive X-ray spectroscopy (STEM-EDS) elemental maps, and aberration-corrected MAADF-STEM images and corresponding EEL point.

Figure 3d illuminates the dynamical structure changes of Co species and the formation of atomically dispersed CoN_4 sties within a nitrogen-doped carbon host as a function of thermal activation temperature: conversion of the Co(II) hydroxide (room temperature) to an oxide-rich mixture of phases up to 523 °C, to CoN_4 with a minor Co metal contribution (~700 °C), and Co-N bond optimization and removal of Co metal (>700 °C). At this temperature, the Co-N coordination number and bond length are similar to those for the Co phthalocyanine standard. The CoN_4 structure was maintained at 1100 ºC even after cooling down to room temperature, indicating that the formed CoN_4 active site over 700 °C is very stable (**Figure S13**). It is noteworthy that this process is quite different from the formation process of FeN_x sites reported previously.[2] That work elucidated that ultrafine FeO_x particles (<2 nm) first formed at a low temperature (**Figure S14**) and then transformed into atomically-dispersed FeN_4 active sites at a relatively lower temperature (400 °C), which are converted to the optimal active FeN_4 coordination and local structure at 700 °C.

Medium-angle annular dark-field (MAADF) images of the ZIF-NC-Co-RT sample shown in **Figure 4a** indicate that the single metal sites are uniformly dispersed in the carbon phases. However, when the electron probe with 1 Å resolution was targeted on the bright metal spots, those metal sites behaved significantly differently. Some single Co sites are stable and are accompanied by N atoms observed in the EEL point spectrum (**Figure S15**), implying that relatively strong Co-N coordination exists even after simple chemical adsorption. In contrast, some single Co sites migrate under the beam, and only a nitrogen signal was detected at the transition metal position, as shown in **Figure 4b** and **Figure S16**. According to XPS results (**Table S4**), these drifting atoms might be ascribed to free Co^{2+} ions, indicating the EELS beam breaks the weak Co-N bonds. With an increase in heating temperatures above 700 °C, the co-existence of Co and N at the atomic level was verified (**Figure 4c-4e**). STEM and EEL point spectroscopy analysis are consistent with the XAS analysis. This indicates that the thermal activation can stabilize the Co-N configuration because Co and N signals were simultaneously detected when placing an electron probe on the isolated bright spot.

2.3 Theoretical studies of thermal-induced Co-N structures

The first principle DFT calculations were performed to elucidate the origin of experimentally observed activity enhancement with the structural evolution of CoN_4 sites at different temperatures. We applied a strained concept for the Co-N bonds in the CoN_4 site based on the distorted active site configuration and shorter Co-N bond lengths discovered from experimental XAS results. Also, we introduced the negative thermal expansion coefficient (TEC) of graphene.[43-46] Therefore, the established model is a distorted nonplanar configuration of CoN_4 active sites formed under elevated temperature. In our previous study on strained FeN_4 active site,[2] we found that some degrees of compressive strain in the FeN_4 moiety would facilitate the *OOH dissociation process and hence kinetically enhance the ORR. Here, we calculated two possible sites: a CoN_4 site embedded in a graphene layer (**Figure 5a**)[2, 6, 47-49] and a CoN_{2+2} active site bridging two graphene edges (**Figure 5b**).[48, 50] The 2% compressively strained CoN_4 site has a nonplanar configuration with shortened Co-N bonds, while the 1.5% compressively strained CoN_{2+2} active site still maintains the planar configuration. Both CoN_4 and CoN_{2+2} sites with compressive strain showed more positive charge accumulation on the central Co atom (**Figure S17**), leading to the stronger binding with O_2 and intermediates.

Moreover, we predicted the optimized configurations of *OOH, *O, and *OH adsorbed on these strained and unstrained CoN_4 and CoN_{2+2} sites (**Figure S18**-**S19**). The corresponding ORR limiting potentials were calculated, which is the maximum applied electrode potential to keep ORR thermodynamically favorable. The variation of ORR limiting potential with the local strain of CoN_4 and CoN_{2+2} active sites is summarized in **Figures 5c** and **5d**. A more positive limiting potential indicates better ORR activity. At the same strained degree, the ORR on the CoN_4 active sites became more thermodynamically favorable relative to the CoN_{2+2} sites.

In contrast, the calculated activation energy for *OOH dissociation on CoN_4 and CoN_{2+2} active sites (**Figure S20**) show the same trend as activation energy is reduced with increasing compressive strain (**Figure 5c-d**). Thus, the ORR activity could be kinetically enhanced on compressively strained CoN_4 and CoN_{2+2} active sites. In particular, as shown in our predicted ORR free energy evolution (**Figure S21**), the applied 2% compressive strain lowered the activation energy for *OOH dissociation from 1.15 eV on unstrained CoN_4 active sites to 1.04 eV. However, all calculated *OOH dissociation activation energies on the CoN_4 active sites are still higher than 1.0 eV, implying a significant difficulty for O-O bond-breaking via *OOH dissociation on these sites. Alternatively, we propose a 2+2 electron pathway involving the adsorption and dissociation of H_2O_2 (**Figure 5e**). The H_2O_2 molecule was predicted not to adsorb on the unstrained CoN_4 sites with only 0.01 eV adsorption energy. However, the adsorption of H_2O_2 is enhanced with adsorption energy changed to -0.09, and -0.11 eV on 1% and 2% compressively strained CoN_4 active site, respectively. The activation energy for H_2O_2 dissociation was predicted to be only 0.11 eV on 2% compressively strained CoN_4 active sites. The ORR is thermodynamically and kinetically favorable *via* *H_2O_2 dissociation on the 2% compressively strained CoN_4 active site (**Figure 5e**). For the CoN_{2+2} active sites, the *OOH dissociation activation energy decreased from 0.59 eV on unstrained sites to 0.43 eV on 1.5% compressively strained sites (**Figure 5f**). However, the predicted limiting potential was also reduced from 0.78 V to 0.55 V. Thus, a small degree of compressive strain in CoN_{2+2} active sites could kinetically facilitate the ORR process by enhancing *OOH dissociation process, but excessive compressive strain would result in thermodynamically unfavorable. The thermal stability of CoN_4 active sites was also investigated (**Figure S22**). The large positive free energy change implies that CoN_4 sites are very stable, and only very high temperatures can initiate N's dissociation from the active sites.

To validate our computational predictions, we have carried out an H_2O_2 reduction experiment using the ZIF-NC-Co-900C catalyst, which usually contains both CoN_4 and CoN_{2+2} sites. **Figure 5g** shows the amperometric responses of H_2O_2 reduction on the catalyst in N_2-saturated 0.5 M H_2SO_4 with the addition of 1.0 mmol H_2O_2 at the indicated time intervals while holding the potential at 0.2 V. This catalyst exhibited a fast amperometric response toward H_2O_2 reduction and achieved steady-state current density. A remarkable increase in current response could be observed with increasing H_2O_2 concentration. The currents scaled linearly with the bulk concentration of H_2O_2 in the region investigated (**Figure 5h**), which is characteristic of a diffusion-limited electrochemical reaction. Therefore, the combined computational and experimental studies suggest that H_2O_2 adsorption on CoN_4 sites and the subsequent reduction to H_2O was kinetically enhanced by the thermally-induced compressive strain in the CoN_4 and CoN_{2+2} active sites, hosted in the atomically dispersed Co-N-C catalyst.

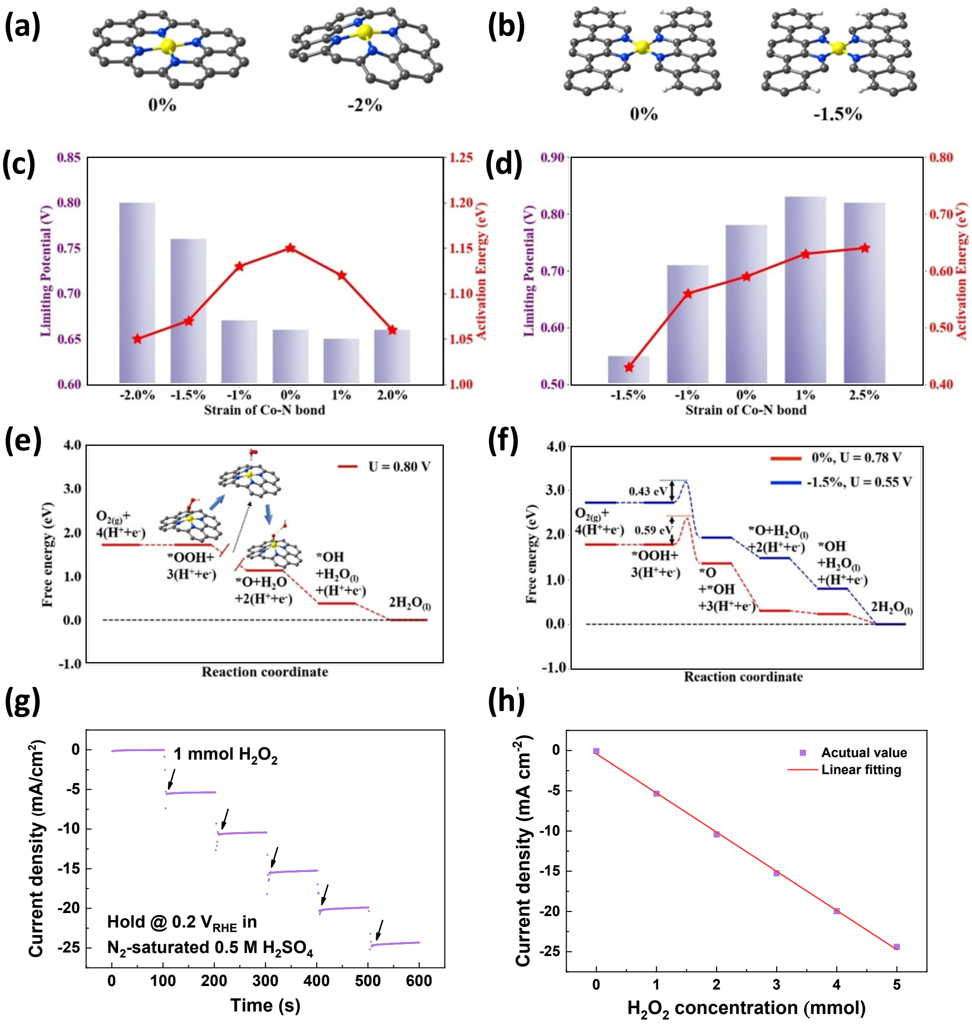

Figure 5. Atomic structures of fully relaxed and compressively strained (a) CoN_4 active site embedded in a graphene layer and (b) CoN_{2+2} active site bridging two graphene edges. The gray, blue, and orange balls represent C, N, and Co atoms, respectively. Predicted limiting the potential of ORR and activation energy for *OOH dissociation on (c) CoN_4 and (d) CoN_{2+2} active sites with varying local strain. (e) Predicted free energy evolution of ORR on 2 % compressed CoN_4 active site through a four-electron pathway via *H_2O_2 dissociation. (f) Predicted free energy evolution of ORR on CoN_{2+2} active sites with no and 1.5% compressive strain through a 4e^- pathway via *OOH dissociation. (g) Amperometric responses of the ZIF-NC-Co-900C catalyst at a constant potential (0.2 V *vs.* RHE) with consecutive addition of 1 mmol H_2O_2 in N_2-saturated 0.5 M H_2SO_4. (h) Calibration curve for the current response to H_2O_2 concentration from 0 to 5 mmol in N_2-saturated 0.5 M H_2SO_4.

2.4 Two-step synthesis for high-efficient Co-N-C catalysts

The understanding of Co-N coordination structural evolution during the thermal activation is critical for rationally designing highly active and efficient Co-N-C catalysts with increased CoN_4 site density and optimal porosity for mass transfer in fuel cells. For example, we can accurately control thermal activation temperatures to realize maximum atomic dispersion of Co sites, and the highest intrinsic ORR activity and 4e^- selectivity on optimal Co-N local strains. On the contrary, we can realize the dominant 2e^- pathway for H_2O_2 generation by controlling a relatively low thermal activation at 300 °C.

Here, we further developed effective approaches to engineering catalyst morphology for improved catalytic performance. Generally, increasing micropore volumes in carbon support could afford additional defects for increased active sites. Mesopores favor a faster mass transfer and enable more active sites exposed to reactants.[51-57] Thus, innovative synthesis methods to facilitate Co-N coordination during the heating treatment and formation of multiscale pore structures are highly desirable for boosting catalytic activity and, especially, fuel cell performance.

In the second part of this work, we developed a two-step chemical doping and ion adsorption method to introduce more CoN_4 sites and optimize the catalyst's pore structure. In the first step, the pre-doped Co species in the carbon host is crucial in creating more micropore and mesopores in Co-N-C catalysts via facilitating Zn's removal from the ZIF-8 precursor during the carbonization to form a carbon host for subsequent ion adsorption (**Figure S23**). The pore-distribution plot, along with the nitrogen adsorption-desorption isothermal curve in **Figure S24-S25** and the pore volume values in **Table S12,** verified the role of pre-coped Co in increasing mesopore volume. Besides, the pre-doped Co slightly enhanced the graphitization degree of the carbon host derived from ZIF-8 precursors (**Figure S26**), which is beneficial for enhancing carbon corrosion resistance and catalyst stability. Furthermore, the pre-Co-doping can significantly reduce the residual Zn amount,[58] providing more N-coordination sites for the subsequent Co ion adsorption. The increased density of active sites in a Co-N-C catalyst via a two-step synthesis (*e.g.*, 1% pre-doping Co and Co adsorption, thermally activated at 900 °C) is verified by higher N and Co content determined by using XPS analysis (**Figure S27**, and **Table S13-S15**).

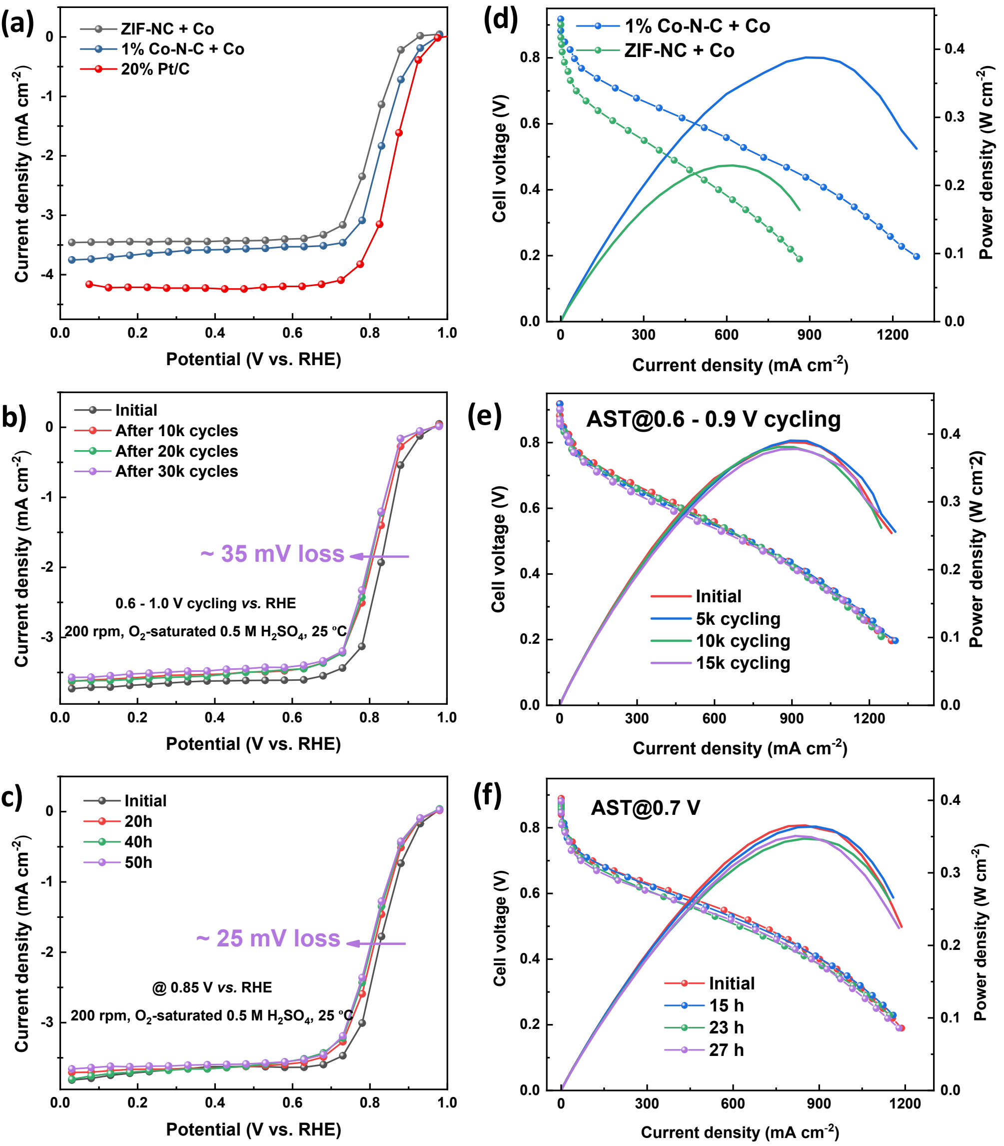

Figure 6. ORR activity was studied by RRDE and fuel cell tests. (a) steady-state ORR polarization plots in 0.5 M H_2SO_4 electrolytes to study the effect of Co^{2+} chemical doping in the carbon hosts. The Pt/C catalyst with 60 μg_{Pt} cm^{-2} was tested in 0.1 M $HClO_4$. Stability study including potentiostatic tests (b) potential cycling from 0.6 to 1.0 V and (c) @ 0.85 V to determine intrinsic stability of Co-N_4 sites in 1% Co-N-C+Co catalyst in 0.5 M H_2SO_4. (d) fuel cell performance of 1% Co-N-C+Co and ZIF-NC+Co catalyst in both H_2/O_2 and H_2/air conditions. Fuel cell stability and durability tests of the best-performing 1% Co-N-C+Co catalyst in an H_2/air cell through (e) voltage cycling between 0.6 V to 0.9 V and (f) potentiostatic test @ 0.7 V with the flow of H_2 and air. Cathode catalyst loading: 4.0 mg cm^{-2}. Cell temperature: 80°C; flow rate H_2/air 200/200 sccm. 100% relative humidity. 1.0 bar H_2/air. Nafion 212.

A series of two-step Co-N-C catalysts with various pre-doped Co contents combined with optimal adsorption and thermal activation at 900 °C were prepared. Their ORR activities were assessed using RDE measurements in an O_2 saturated 0.5 M H_2SO_4 electrolyte (**Figure S28** and **Figure 6a**). The best-performing two-step Co-N-C catalyst from 1.0% Co pre-doping exhibited an E_{onset} of 0.97 V and an $E_{1/2}$ of 0.83 V with a regular catalyst loading of 0.6 mg cm^{-2}, which was *ca*. 30 mV positive of the one-step ZIF-NC-Co-900 without Co pre-doping. It is only *ca.* 40 mV negative to the commercial Pt/C (*e.g.*, 0.87 V) with Pt loading of 60 µg cm^{-2}. The ORR activity is exceptional when compared to other reported Co-N-C catalysts (**Figure S29**). The enhanced ORR activity measured with the two-step Co-N-C catalyst is contributed to the increased density of CoN_4 active sites through this pre-doping method according to the XPS analysis (**Figure S30**). In particular, N and Co contents of the two-step 1%Co-N-C+Co catalyst is increased to 3.9 and 0.6 at.%, respectively, when compared to the one-step ZIF-NC-Co catalyst (3.2 and 0.4 at.%). The RDE tests of these 1%Co-N-C+Co-T catalysts, treated at different temperatures, verified the importance of thermal activation temperature, consistent with the studies for one-step Co-N-C catalysts (**Figure S31**). The best performing catalyst was obtained at 900 °C, corresponding to the highest intrinsic activity. Even before the second adsorption step, ORR activities of all 1%Co-N-C+Co-T catalysts are higher than corresponding one-step catalysts. The improved ORR activity is due to the increased CoN_4 active sites and more favorable pore structures.

Notably, we also performed *ex-situ* XAS for these two-step 1%Co-N-C+Co-T catalysts (**Figure S32-34**), verifying the exclusive CoN_4 site formation in catalysts. These two-step synthesized samples showed a similar Co speciation evolution trend as observed for the one-step method, but required higher temperature, 1000 °C *vs*. 800 °C, to convert all Co to CoN_4 species. The different behaviors are due to the nature of *ex-situ* and *in situ* XAS experiments. Also, likely, the pre-doped CoN_4 sites in the catalyst (in the first step) inhibit the diffusion of adsorbed Co ions (in the second step) from coordinating with N dopants. It might be more valuable to study the CoN_x evolution of the two-step Co-N-C catalyst through *in situ* XAS experiments. However, it may generate several confusions for illustrating the overall structural change. The pre-doped Co atoms may cause the concurrent changing of nitrogen doping, graphitization, and local carbon structure with increasing thermal activation temperatures (**Figure S24-S27**). Therefore, it is challenging to precisely and exclusively determine Co-N bonds and their intrinsic effects on ORR activity in the complicated two-step catalyst systems.

The two-step Co-N-C catalyst exhibited excellent long-term durability, only losing 35 mV of $E_{1/2}$ (**Figure 6b**) after a 30,000-cycle accelerated stress test (AST) cycling from 0.6 to 1.0 V. The current density after holding at 0.85 V for 50 hours retained around 80% and only lost 25 mV in $E_{1/2}$, (**Figure 6c** and **S35),** indicating promising stability in acidic media. In contrast, the degradation of the one-step ZIF-NC-Co-900 catalyst is 45 mV in $E_{1/2}$ after 30 000 potential cycles (**Figure S36**). Thus, the pre-doping step can yield a high degree of graphitization that effectively improves catalyst stability.

The two-step Co-N-C catalyst was further integrated into membrane electrode assemblies (MEAs) for evaluating its fuel cell performance (**Table S16**). The MEA was tested in an H_2-O_2 cell first to evaluate catalyst performance with minimum mass-transport losses (**Figure S37**). The MEA exhibited an open circuit voltage (OCV) of 0.94 V and a peak power density of 0.73 W cm^{-2}, which is much higher than the one-step Co-N-C cathode catalyst (*i.e.*, ZIF-NC+Co, 0.87 V and 0.50 W cm^{-2}). The two-step Co-N-C catalyst cathode generated an increased current density of 60 mA cm^{-2} at 0.8 V (**Figure 6d**), which is six-times higher than that of the one-step catalyst (*i.e.*, 9.5 mA cm^{-2}), clearly affirming the importance of pre-doping of Co during the two-step synthesis. Under more practical H_2-air conditions, the peak power density is 0.39 W cm^{-2}, much higher than 0.23 W cm^{-2} for the one-step catalyst and other reported Co-N-C catalysts (**Figure S38**). The improved mass transport behavior also verified the benefit of pore structure resulting from the Co pre-doping.

Subsequently, the long-term durability test of the two-step Co-N-C cathode in MEA was evaluated using multiple test protocols. During the extensive ASTs by voltage cycling (0.6 to 0.9 V) in H_2-air condition, the voltage drop at a current density of 0.8 A cm^{-2} was only 10 mV after 15,000 cycles, likely achieving the DOE target of <30 mV loss (after 30,000 cycles), as shown in **Figure 6e**. The durability test was also evaluated by holding the H_2-air cell at a constant cell voltage of 0.7 V. After the 27-hour test (**Figure 6f** and **S39**), ~67 % of the current density was retained, and a 20 mV voltage loss at 0.8 A cm^{-2} was noted in recorded polarization plots. The encouraging stability is due to the inherent Co-N bond stability at optimal thermal activation and the enhanced carbon corrosion resistance. The mitigated carbon corrosion is attributed to the eliminated Fenton reaction by using Fe-free catalysts and increased graphitization degree of the carbon host due to the pre-doped Co as evidenced by the Raman analysis. Therefore, the two-step chemical-doping and ion adsorption method effectively increases the density of active sites, optimizes the mesopore volume for facilitating the mass transfer, exposes more active sites, and enhances carbon corrosion resistance in the Co-N-C catalysts.

Conclusion

In summary, we elucidate CoN_4 active site formation mechanism using ZIF-8 derived N-doped carbon as the ideal host for Co ion adsorption, followed by thermal activation at different temperatures. The structural evolution of the CoN_4 site under controlled heat treatment was monitored via *in situ* XAS characterization along with atomic-level electron microscopy. *In situ* XAS analysis showed the evolution process of the Co-containing species, which the Co hydroxide at room temperature undergoes dehydration/decomposition to form an oxide-rich mixture of phases up to 523 °C, to CoN_4 with a minor Co metal contribution at ~700 °C, and entirely to atomically dispersed CoN_4 active sites at >800 °C. While Co-N bond could be formed at room temperature after chemical adsorption, 700 °C is the critical point to create ORR active CoN_4 sites, and >800 °C is the optimal temperature for the complete transition. The formation of CoN_4 sites requires larger thermal energy, *i.e.,* higher formation temperatures at 700 °C than the FeN_4 site formed at a relatively low temperature of 400°C.[2] DFT calculations further elucidated that ORR was kinetically enhanced by the thermal-induced compressive strain of Co-N bonds in CoN_4 and CoN_{2+2} active sites. The thermodynamics of ORR become more favorable on the compressively strained CoN_4 active sites. The strain concept for CoN_4 sites well explained the enhanced ORR activity with an increase of heating temperature up to 900 °C. The theoretical computation elucidates that low H_2O_2 yields were determined in the Co-N-C catalysts, which is due to the strained CoN_4 sites' high activity for the H_2O_2 reduction via the 2+2e^- pathway for the ORR.

Furthermore, the new understanding of Co-N coordination structural changes motivated us to design effective catalyst systems for fuel cells. We developed a two-step Co-N-C catalyst by combining chemical Co-doping into ZIF-8 precursors and the subsequent Co ion adsorption to the ZIF-8 derived carbon host. Exceptional ORR activity and stability in acidic media were achieved on the two-step Co-N-C catalyst. Moreover, MEAs with the Co-N-C cathode catalyst displayed encouraging H_2-air cell performance with a peak power density of 0.39 W cm^{-2}, together with excellent stability under various AST protocols. The remarkably enhanced performance can be attributed to the optimal local Co-N coordination, the increased density of CoN_4 active sites, optimized porosity with favorable mass transfer, and enhanced carbon corrosion resistance. Thus, in addition to providing a fundamental understanding of Co-N coordination structural changes during the CoN_4 site formation, we also developed an effective approach to designing advanced Co-N-C catalysts for fuel cells with enhanced performance and durability.

Acknowledgments

The authors acknowledge the U.S. Department of Energy, Energy Efficiency and Renewable Energy, Hydrogen and Fuel Cell Technologies Office (DOE-EERE-HFTO) through the Electrocatalysis Consortium (ElectroCat) and the DOE program managers, Dimitrios Papageorgopoulos and David Peterson. Argonne National Laboratory's work is supported by DOE-EERE-HFTO under contract DE-AC02-06CH11357. The XAS experiments were performed at the Advanced Photon Source (APS), a DOE Office of Science User Facility operated for the DOE Office of Science by Argonne National Laboratory, also under Contract No. DE-AC02-06CH11357. The operation of MRCAT at the APS is supported by the DOE the MRCAT member institutions. G. Wu also thank the support from National Science Foundation (CBET-1604392, 1804326).

Keywords: Single metal site • Co-N-C • in-situ XAS • oxygen reduction reaction • fuel cells

References

[1] X. X. Wang, M. T. Swihart, G. J. N. C. Wu, *Nature Catalysis* **2019**, *2*, 578.

[2] J. Li, H. Zhang, W. Samarakoon, W. Shan, D. A. Cullen, S. Karakalos, M. Chen, D. Gu, K. L. More, G. Wang, Z. Feng, Z. Wang, G. Wu, *Angewandte Chemie International Edition* **2019**, *58*, 18971-18980.

[3] D. Banham, J.-Y. Choi, T. Kishimoto, S. Ye, *Advanced Materials* **2019**, *31*, 1804846.

[4] M. Xiao, Y. Chen, J. Zhu, H. Zhang, X. Zhao, L. Gao, X. Wang, J. Zhao, J. Ge, Z. Jiang, S. Chen, C. Liu, W. Xing, *Journal of the American Chemical Society* **2019**, *141*, 17763-17770.

[5] F. Pan, H. Zhang, K. Liu, D. Cullen, K. More, M. Wang, Z. Feng, G. Wang, G. Wu, Y. Li, *ACS Catalysis* **2018**, *8*, 3116-3122.

[6] N. Mohd Adli, W. Shan, S. Hwang, W. Samarakoon, S. Karakalos, Y. Li, D. A. Cullen, D. Su, Z. Feng, G. Wang, G. Wu, *Angewandte Chemie International Edition* **2021**, *60*, 1022-1032.

[7] Y. Li, H. Wang, C. Priest, S. Li, P. Xu, G. Wu, *Advanced Materials* **2020**, 2000381.

[8] Q. Shi, S. Hwang, H. Yang, F. Ismail, D. Su, D. Higgins, G. Wu, *Materials Today* **2020**, *37*, 93-111.

[9] Y. Zhu, J. Sokolowski, X. Song, Y. He, Y. Mei, G. Wu, *Advanced Energy Materials* **2020**, *10*, 1902844.

[10] Y. Wang, H. Su, Y. He, L. Li, S. Zhu, H. Shen, P. Xie, X. Fu, G. Zhou, C. Feng, D. Zhao, F. Xiao, X. Zhu, Y. Zeng, M. Shao, S. Chen, G. Wu, J. Zeng, C. Wang, *Chemical Reviews* **2020**, *120*, 12217-12314.

[11] M. Chen, Y. He, J. S. Spendelow, G. Wu, *ACS Energy Letters* **2019**, *4*, 1619-1633.

[12] H. Zhang, S. Hwang, M. Wang, Z. Feng, S. Karakalos, L. Luo, Z. Qiao, X. Xie, C. Wang, D. Su, Y. Shao, G. Wu, *Journal of the American Chemical Society* **2017**, *139*, 14143-14149.

[13] U. Martinez, S. Komini Babu, E. F. Holby, H. T. Chung, X. Yin, P. Zelenay, *Advanced Materials* **2019**, *31*, 1806545.

[14] Y. He, S. Liu, C. Priest, Q. Shi, G. Wu, *Chemical Society Reviews* **2020**, *49*, 3484-3524.

[15] H. Zhang, H. T. Chung, D. A. Cullen, S. Wagner, U. I. Kramm, K. L. More, P. Zelenay, G. Wu, *Energy & Environmental Science* **2019**, *12*, 2548-2558.

[16] M. Xiao, J. Zhu, L. Ma, Z. Jin, J. Ge, X. Deng, Y. Hou, Q. He, J. Li, Q. Jia, S. Mukerjee, R. Yang, Z. Jiang, D. Su, C. Liu, W. Xing, *ACS Catalysis* **2018**, *8*, 2824-2832.

[17] T. Asset, P. Atanassov, *Joule* **2020**, *4*, 33-44.

[18] S. Liu, Q. Shi, G. Wu, *Nature Catalysis* **2021**, *4*, 6-7.

[19] J. Li, M. Chen, D. A. Cullen, S. Hwang, M. Wang, B. Li, K. Liu, S. Karakalos, M. Lucero, H. Zhang, C. Lei, H. Xu, G. E. Sterbinsky, Z. Feng, D. Su, K. L. More, G. Wang, Z. Wang, G. Wu, *Nature Catalysis* **2018**, *1*, 935-945.

[20] M. Chen, X. Li, F. Yang, B. Li, T. Stracensky, S. Karakalos, S. Mukerjee, Q. Jia, D. Su, G. Wang, G. Wu, H. Xu, *ACS Catalysis* **2020**, *10*, 10523-10534.

[21] K. Liu, Z. Qiao, S. Hwang, Z. Liu, H. Zhang, D. Su, H. Xu, G. Wu, G. Wang, *Applied Catalysis B: Environmental* **2019**, *243*, 195-203.

[22] C. H. Choi, H.-K. Lim, M. W. Chung, G. Chon, N. Ranjbar Sahraie, A. Altin, M.-T. Sougrati, L. Stievano, H. S. Oh, E. S. Park, F. Luo, P. Strasser, G. Dražić, K. J. J. Mayrhofer, H. Kim, F. Jaouen, *Energy & Environmental Science* **2018**, *11*, 3176-3182.

[23] S.-F. Kang, H.-M. Chang, *Water Science and Technology* **1997**, *36*, 215-222.

[24] E. F. Holby, G. Wang, P. Zelenay, *ACS Catalysis* **2020**, *10*, 14527-14539.

[25] X. X. Wang, V. Prabhakaran, Y. He, Y. Shao, G. Wu, *Advanced Materials* **2019**, *31*, 1805126.

[26] M. Xiao, H. Zhang, Y. Chen, J. Zhu, L. Gao, Z. Jin, J. Ge, Z. Jiang, S. Chen, C. Liu, W. Xing, *Nano Energy* **2018**, *46*, 396-403.

[27] X. Xie, C. He, B. Li, Y. He, D. A. Cullen, E. C. Wegener, A. J. Kropf, U. Martinez, Y. Cheng, M. H. Engelhard, M. E. Bowden, M. Song, T. Lemmon, X. S. Li, Z. Nie, J. Liu, D. J. Myers, P. Zelenay, G. Wang, G. Wu, V. Ramani, Y. Shao, *Nature Catalysis* **2020**, *3*, 1044-1054.

[28] Y. He, S. Hwang, D. A. Cullen, M. A. Uddin, L. Langhorst, B. Li, S. Karakalos, A. J. Kropf, E. C. Wegener, J. Sokolowski, M. Chen, D. Myers, D. Su, K. L. More, G. Wang, S. Litster, G. Wu, *Energy & Environmental Science* **2019**, *12*, 250-260.

[29] X. X. Wang, D. A. Cullen, Y.-T. Pan, S. Hwang, M. Wang, Z. Feng, J. Wang, M. H. Engelhard, H. Zhang, Y. He, Y. Shao, D. Su, K. L. More, J. S. Spendelow, G. Wu, *Advanced Materials* **2018**, *30*, 1706758.

[30] L. Chen, X. Liu, L. Zheng, Y. Li, X. Guo, X. Wan, Q. Liu, J. Shang, J. Shui, *Applied Catalysis B: Environmental* **2019**, *256*, 117849.

[31] L. Chong, G. A. Goenaga, K. Williams, H. M. Barkholtz, L. R. Grabstanowicz, J. A. Brooksbank, A. B. Papandrew, R. Elzein, R. Schlaf, T. A. Zawodzinski Jr, J. Zou, S. Ma, D.-J. Liu, *ChemElectroChem* **2016**, *3*, 1541-1545.

[32] Y. He, H. Guo, S. Hwang, X. Yang, Z. He, J. Braaten, S. Karakalos, W. Shan, M. Wang, H. Zhou, Z. Feng, K. L. More, G. Wang, D. Su, D. A. Cullen, L. Fei, S. Litster, G. Wu, *Advanced Materials* **2020**, *32*, 2003577.

[33] Y. Chen, R. Gao, S. Ji, H. Li, K. Tang, P. Jiang, H. Hu, Z. Zhang, H. Hao, Q. Qu, X. Liang, W. Chen, J. Dong, D. Wang, Y. Li, *Angewandte Chemie International Edition* **2020**, 10.1002/anie.202012798.

[34] Y. Ha, B. Fei, X. Yan, H. Xu, Z. Chen, L. Shi, M. Fu, W. Xu, R. Wu, *Advanced Energy Materials* **2020**, *10*, 2002592.

[35] Y. Shao, J.-P. Dodelet, G. Wu, P. Zelenay, *Advanced Materials* **2019**, *31*, 1807615.

[36] Q. Cheng, L. Yang, L. Zou, Z. Zou, C. Chen, Z. Hu, H. Yang, *ACS Catalysis* **2017**, *7*, 6864-6871.

[37] W. Gong, Y. Lin, C. Chen, M. Al-Mamun, H.-S. Lu, G. Wang, H. Zhang, H. Zhao, *Advanced Materials* **2019**, *31*, 1808341.

[38] G. Wu, A. Santandreu, W. Kellogg, S. Gupta, O. Ogoke, H. Zhang, H.-L. Wang, L. Dai, *Nano Energy* **2016**, *29*, 83-110.

[39] G. Wu, C. M. Johnston, N. H. Mack, K. Artyushkova, M. Ferrandon, M. Nelson, J. S. Lezama-Pacheco, S. D. Conradson, K. L. More, D. J. Myers, P. Zelenay, *Journal of Materials Chemistry* **2011**, *21*, 11392-11405.

[40] G. Wu, K. L. More, C. M. Johnston, P. Zelenay, *Science* **2011**, *332*, 443-447.

[41] J. Hong, E. Marceau, A. Y. Khodakov, A. Griboval-Constant, C. La Fontaine, V. Briois, *Chemistry – A European Journal* **2012**, *18*, 2802-2805.

[42] A. Zitolo, N. Ranjbar-Sahraie, T. Mineva, J. Li, Q. Jia, S. Stamatin, G. F. Harrington, S. M. Lyth, P. Krtil, S. Mukerjee, E. Fonda, F. Jaouen, *Nature Communications* **2017**, *8*, 957.

[43] N. Mounet, N. Marzari, *Physical Review B* **2005**, *71*, 205214.

[44] W. Bao, F. Miao, Z. Chen, H. Zhang, W. Jang, C. Dames, C. N. Lau, *Nature Nanotechnology* **2009**, *4*, 562-566.

[45] M. Pozzo, D. Alfè, P. Lacovig, P. Hofmann, S. Lizzit, A. Baraldi, *Physical Review Letters* **2011**, *106*, 135501.

[46] D. Yoon, Y.-W. Son, H. Cheong, *Nano Letters* **2011**, *11*, 3227-3231.

[47] K. Liu, S. Kattel, V. Mao, G. Wang, *The Journal of Physical Chemistry C* **2016**, *120*, 1586-1596.

[48] K. Liu, G. Wu, G. Wang, *The Journal of Physical Chemistry C* **2017**, *121*, 11319-11324.

[49] S. Mukherjee, X. Yang, W. Shan, W. Samarakoon, S. Karakalos, D. A. Cullen, K. More, M. Wang, Z. Feng, G. Wang, *Small Methods* **2020**, *4*, 1900821.

[50] M. Lefèvre, E. Proietti, F. Jaouen, J.-P. Dodelet, *Science* **2009**, *324*, 71-74.

[51] X. Wan, X. Liu, Y. Li, R. Yu, L. Zheng, W. Yan, H. Wang, M. Xu, J. Shui, *Nature Catalysis* **2019**, *2*, 259-268.

[52] H. Yang, Q. Lin, Y. Wu, G. Li, Q. Hu, X. Chai, X. Ren, Q. Zhang, J. Liu, C. He, *Nano Energy* **2020**, *70*, 104454.

[53] A. Uddin, L. Dunsmore, H. Zhang, L. Hu, G. Wu, S. Litster, *ACS Applied Materials & Interfaces* **2019**, *12*, 2216-2224.

[54] J. Shui, C. Chen, L. Grabstanowicz, D. Zhao, D.-J. Liu, *Proceedings of the National Academy of Sciences* **2015**, *112*, 10629-10634.

[55] S. H. Lee, J. Kim, D. Y. Chung, J. M. Yoo, H. S. Lee, M. J. Kim, B. S. Mun, S. G. Kwon, Y.-E. Sung, T. Hyeon, *Journal of the American Chemical Society* **2019**, *141*, 2035-2045.

[56] S. Liu, M. Wang, X. Yang, Q. Shi, Z. Qiao, M. Lucero, Q. Ma, K. L. More, D. A. Cullen, Z. Feng, G. Wu, *Angewandte Chemie International Edition* **2020**, *59*, 21698-21705.

[57] X. Zhao, X. Yang, M. Wang, S. Hwang, S. Karakalos, M. Chen, Z. Qiao, L. Wang, B. Liu, Q. Ma, D. A. Cullen, D. Su, H. Yang, H.-Y. Zang, Z. Feng, G. Wu, *Applied Catalysis B: Environmental* **2020**, *279*, 119400.

[58] Q. Shi, Y. He, X. Bai, M. Wang, D. A. Cullen, M. Lucero, X. Zhao, K. L. More, H. Zhou, Z. Feng, Y. Liu, G. Wu, *Energy & Environmental Science* **2020**, *13*, 3544-3555.

Table of Contents

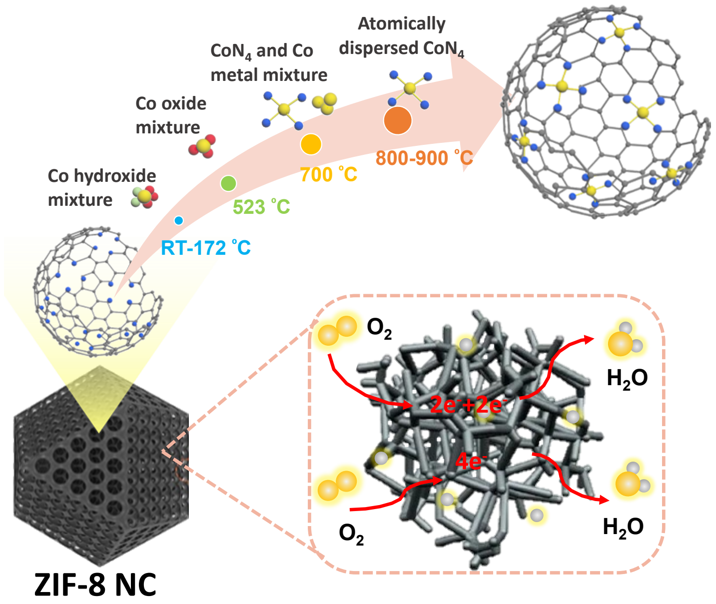

In situ high-tempeature X-ray absorption spectroscopy along with atomic level electron microscopy were developed to monitor the structural evolution of the CoN$_4$ site during the thermal activation to elucidate the formation mechanism. 700°C is a critical temperature to convert inactive Co oxides and metals to active CoN$_4$ sites, and 900 °C is optimal to complete the conversion and yield the Co-N bond for the highest intrinsic activity and four-electron selectivity. Theoretical calculations elucidate that the temperature-dependent activity is due to the compressive strain on Co-N bonds with favorable thermodynamics and kinetics for the ORR. Motived with the new understanding, a two-step Co-N-C catalyst was designed via a chemical doping and ion adsorption strategy, showing significantly enhanced activity, stability, and fuel cell performance.